Pulse sequences for controlled two- and three-qubit gates in a hybrid quantum register

Jingfu Zhang, Swathi S. Hegde, and Dieter Suter

Fakultät Physik, Technische Universität Dortmund, D-44221 Dortmund, Germany

We propose and demonstrate a quantum control scheme for hybrid quantum registers that can reduce the operation time, and therefore the effects of relaxation, compared to existing implementations. It combines resonant excitation pulses with periods of free precession under the internal Hamiltonian of the qubit system. We use this scheme to implement quantum gates like controlled-NOT operations on electronic and nuclear spins of the nitrogen-vacancy center in diamond. As a specific application, we transfer population between electronic and nuclear spin qubits and use it to measure the Rabi oscillations of a nuclear spin in a system with multiple coupled spins.

I. INTRODUCTION

High-precision quantum control is required in various fields, such as quantum computing [1–3]. The gate operations used for quantum control often rely on resonant electromagnetic fields that drive the targeted qubits near a resonant transition. While this drive operation should be strong, to dominate over unwanted effects and to allow short gate operations, the strength of the control field is often also limited by the requirement that it must not affect qubits that are not targeted in the specific operation.

Meeting these requirements becomes progressively more challenging as the number of qubits increases, as larger systems have more resonant transitions that must be considered. In many systems, the strengths of the couplings between the qubits, which are essential for multiqubit gates, cover a significant range of values. Examples include hybrid quantum registers for quantum computing, such as the nitrogen-vacancy (NV) center in diamond, where the couplings between the electron and ^{13}C spins can be in a range from less than 0.1 MHz to 130 MHz [4–6]. If the couplings are weak, the duration of the gate operations that rely on these interactions increases correspondingly. Implementations of multiqubit operations often rely on transition selective (also called line selective or soft) pulses [6–10], which are designed to drive only a single transition with a resonant field. As a result, however, this method is limited by the spectral resolution, because the driving field must be weak compared to the separations of this transition from the others, which are usually determined by strength of the coupling constants. Under this condition, the effective fields acting on the off-resonant transitions are nearly perpendicular to the control field, and therefore they remain virtually unaffected [11–14]. However, this condition may be in conflict with the requirement that the gate operation should be fast compared to the relaxation time.

To avoid this conflict, we propose and demonstrate here an alternative approach, which is often used in liquid-state magnetic resonance but less frequently in solid-state systems like the diamond NV center [4]. It is based on combining hard pulses, i.e., driving fields that are strong compared to the

couplings, with periods of free precession, where the coupling differentiates between the different qubit states. The gate durations are mainly determined by the coupling strengths between the qubits, and we can obtain the minimum possible duration for the given system, which can be much shorter than with transition-selective pulses. Moreover, our technique also offers the possibility to combine the pulses with techniques for reducing decoherence [15], such as dynamical decoupling. In particular, dynamical decoupling pulses can be combined with gate operations for designing gates that are protected against environmental noise [8,16].

In the following sections, we first discuss the implementation of these controlled gates for the electron and ^{14}N system in Sec. II. In Sec. III, we consider a three-spin system and describe some experiments based on controlled gates, for measuring the Rabi frequencies of ^{14}N. In Sect. IV, we discuss the implementation of a controlled-controlled NOT (CCNOT) gate in the three spin system consisting of the electron ^{14}N and ^{13}C. In Sect. V, we investigate the dependence of the controlled gates on the offsets of the MW frequency. The experiments were performed at room temperature, using two diamond samples: one has natural abundance, with ∼1.1% ^{13}C, and the other is ^{12}C enriched to 99.995%.

II. ELECTRON SPIN + ^{14}N NUCLEAR SPIN

A. Hamiltonian

The system that we consider consists of the electron spin and the ^{14}N nuclear spin system of a single NV center. If the magnetic field is oriented along the NV symmetry axis, the relevant Hamiltonian can be written as [4,17]

$$\frac{1}{2\pi}\mathcal{H}_{E,N} = DS_z^2 - \gamma_e BS_z + PI_z^2 - \gamma_n BI_z + AS_zI_z. \quad (1)$$

Here S_z and I_z are z-components of the spin-1 operators for the electronic and nuclear spins, respectively. The zero-field splitting is $D = 2.87$ GHz, the nuclear quadrupolar splitting is $P = -4.95$ MHz, and the hyperfine coupling $A = -2.16$ MHz [17–19]. The electronic gyromagnetic ratio is $\gamma_e = -28$ GHz/T and the nuclear gyromagnetic ratio
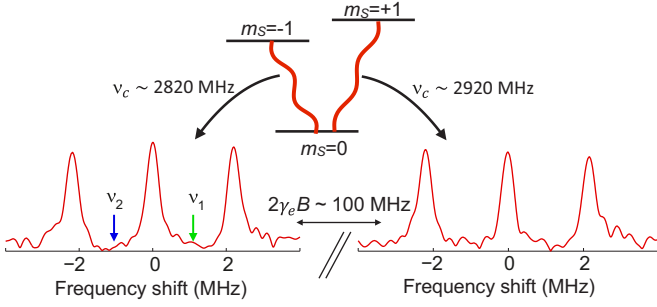
FIG. 1. Energy-level system and spectra of the ESR transitions between the states with $m_S = 0$ and ∓ 1, obtained as Fourier-transforms of time-domain signals. The origins of the frequency axes are set to $D \pm \gamma_e B$. The vertical arrows indicate the carrier frequencies $\nu_{1,2}$ for the MW pulses to implement the conditional operations U_1 and U_2, respectively.

$\gamma_n = 3.1$ MHz/T. In the experiments, the static field strength is about 1.8 mT, which results in a separation of the two electron spin resonance (ESR) transitions by about 100 MHz. Figure 1 shows the spectra of the ESR transitions between the states with $m_S = 0$ and ∓ 1, obtained in Ramsey-type free-induction decay (FID) time-resolved experiments, using resonant MW pulses with Rabi frequencies of about 10 MHz for excitation and detection.

Since the experimental Rabi frequency is small compared to the separation of the two ESR transitions, the individual experiments are confined to a subspace of the full Hilbert space. We consider here the six-dimensional subspace spanned by the states

$$\{|0\rangle_e, |-1\rangle_e\} \otimes \{|1\rangle_n, |0\rangle_n, |-1\rangle_n\}, \tag{2}$$

which is associated to the ESR transition between $|0\rangle_e$ and $|-1\rangle_e$, with a transition frequency $D + \gamma_e B \sim 2820$ MHz. It thus contains one qubit (electron spin; target qubit) and one qutrit (^{14}N spin; control qutrit). The relevant Hamiltonian is then

$$\frac{1}{2\pi}\mathcal{H}^{\text{eff}}_{E,N} = \frac{\nu}{2}\sigma_z \otimes E_3 + \frac{A}{2}\sigma_z \otimes I_z, \tag{3}$$

written in the frame rotating at the MW frequency ν_c. σ_z denotes the z component of the Pauli matrix for the pseudospin $1/2$ of the electron spin in the space $\{|0\rangle_e, |-1\rangle_e\}$, E_3 the identity operator in three dimensions, and

$$\nu = (D + \gamma_e B) - \nu_c \tag{4}$$

is the effective transition frequency of the electron spin qubit in the rotating frame. In addition, the interaction representation also eliminates the quadrupole and Zeeman interactions of the ^{14}N nuclear spin, which are irrelevant for the purpose of this work.

B. Unitary gate operations

The basic MW pulse sequence for a controlled operation is illustrated in Fig. 2. It consists of two $\pi/2$ pulses with a $\pi/2$ relative phase shift, separated by a period τ of free precession, during which the hyperfine interaction causes differential precession, depending on the state of the
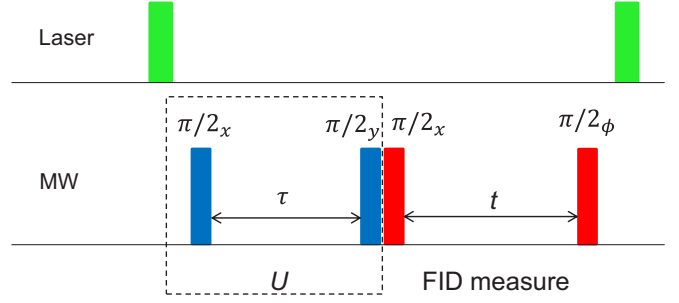

FIG. 2. Pulse sequence for demonstrating the controlled operation U in the electron-^{14}N system. The standard FID measurement is used to monitor the effects of the gate. The phase $\phi = 2\pi \nu_d t$ of the detection pulse is incremented linearly in time to generate an effective offset ν_d. The carrier frequencies of the pulses in U and FID are ν_c and $D + \gamma_e B$, respectively.

nuclear spin. It is closely analogous to sequences used in nuclear magnetic resonance (NMR) quantum computing for implementing controlled-NOT (CNOT) gates [20] and in ENDOR for polarizing the nuclear spin [19]. In the chosen reference frame, the unitary operation generated by the pulse sequence is

$$U = -\frac{i}{2\sqrt{2}}[(c_-(\sigma_z - iE_2) + c_+(\sigma_x + \sigma_y)] \otimes [\sin(\pi A \tau)]I_z$$

$$+ \frac{i}{2\sqrt{2}}[c_+(\sigma_z - iE_2) - c_-(\sigma_x + \sigma_y)]$$

$$\otimes \{[\cos(\pi A \tau) - 1]I_z^2 + E_3\}, \tag{5}$$

with $c_\pm = \cos(\pi \nu \tau \pm \frac{\pi}{4})$. To obtain Eq. (5), we used

$$e^{-i\theta\sigma_z I_z} = -i\sin\theta\sigma_z I_z + [\cos\theta - 1]E_2 \otimes I_z^2 + E_2 \otimes E_3 \tag{6}$$

and assumed that the MW pulses are ideal, with duration zero.

If the free precession period is $\tau = 1/(2|A|)$, the resulting operation U is a conditional qubit-qutrit operation. Examples include the operations U_1 and U_2, which are obtained if the carrier frequency ν_c of the MW pulses is $\nu_1 = D + \gamma_e B - A/2$ and $\nu_2 = D + \gamma_e B + A/2$, respectively. In Fig. 1, these frequencies are indicated by arrows. Table I summarizes the effects of U_1 and U_2 on the basis states of the system. Up to some phase factors, they represent CNOT gates, with the nuclear spin as the control qutrit and the electronic spin as the target qubit.

TABLE I. Output states m_S and m_I of U_1 and U_2 for the system consisting of one qubit (electron S; target) and one qutrit (nuclear spin I; control). Global phase factors have been ignored.

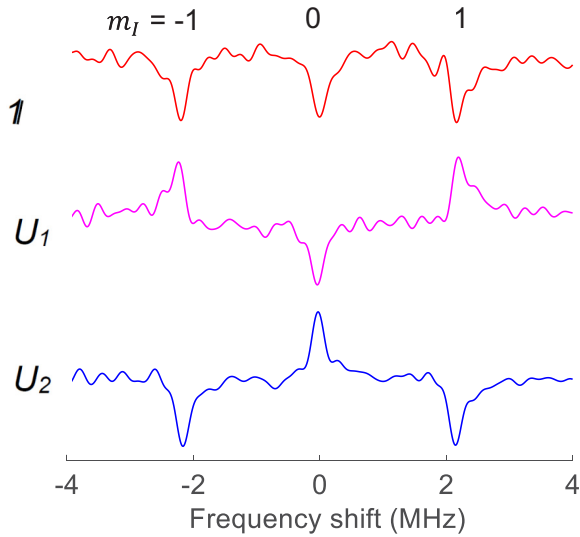| Input	Output of U_1	Output of U_2
0 1	−1 1	0 1
0 0	0 0	−1 0
0 −1	−1 −1	0 −1
−1 1	0 1	−1 1
−1 0	−1 0	0 0
−1 −1	0 −1	−1 −1

FIG. 3. Experimental ESR spectra obtained as Fourier-transforms of the FIDs, after applying the identity **1** (top), U_1 (middle), and U_2 (bottom) gate operations. The quantum numbers above the spectra indicate the states of ^{14}N corresponding to the peaks.

C. Experimental implementation

The experiments were performed in a type-IIa diamond single crystal with a nitrogen concentration less than 5 ppb [21,22], and natural abundance, i.e., ^{13}C concentration ∼1.1%. The NV center can be optically addressed by a green solid-state laser and a home-built confocal microscope [8]. We chose a NV center without resolved ^{13}C hyperfine interaction, as illustrated by the spectra in Fig. 1. The more remote ^{13}C spins cause loss of coherence of the electron spin [23,24], resulting in a transverse relaxation time T_2^* of ≈2.5 μs, measured in a Ramsey-type FID experiment. Figure 2 shows the pulse sequence of the complete experiment.

We first initialized the electron spin into the $m_S = 0$ state by a laser pulse. To a first approximation, the nuclear spin is not affected by the laser pulse but remains unpolarized. Therefore, the state of the two spins after the laser pulse is

$$\rho_{ini} = |0\rangle\langle 0| \otimes \frac{E_3}{3}, \qquad (7)$$

where E_3 denotes the 3×3 unit operator. To this state, we applied the gate operations U, followed by an FID experiment to determine the resulting state of the system. Figure 3 shows the experimental ESR spectra obtained as the Fourier-transforms of the FID. The uppermost trace shows the normal spectrum, i.e., without any gate operation; the second and third trace were obtained after applying the gates U_1 and U_2. Compared with the first trace, which serves as the reference spectrum, the signs of the peaks show that the electron spin states were reversed if the ^{14}N nuclear spin was in the $m_I = \pm 1$ state (for U_1) or in the $m_I = 0$ state (for U_2), as expected from Table I. Minor changes in the shapes of the peaks appear to be due to environmental noise and small shifts can be attributed to magnetic field changes due to thermal drift [25].
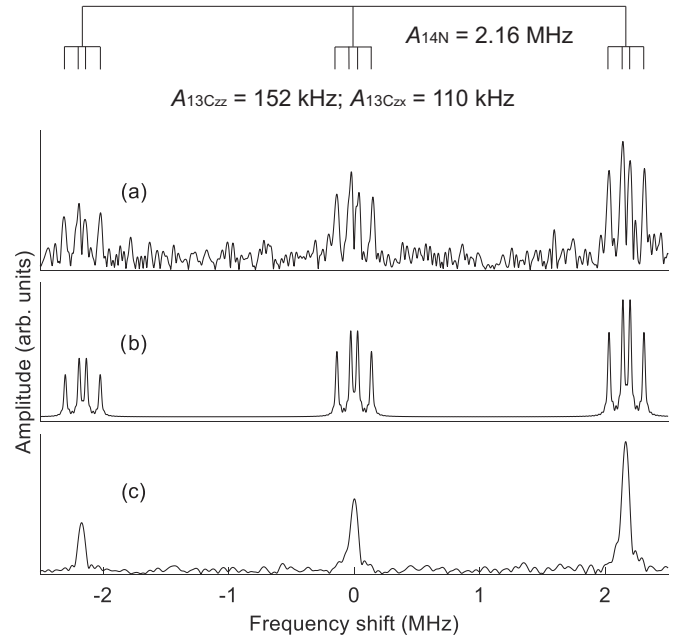

FIG. 4. Spectra of the electron spin coupled to one ^{14}N and one ^{13}C nucleus, obtained from an FID experiment (a) and the corresponding simulation (b). The origin of the frequency axis is $D + \gamma_e B$, corresponding the ESR transition frequency between states $m_S = 0$ and $m_S = -1$. Due to the hyperfine coupling with the ^{13}C nucleus, each peak of the electron-^{14}N system is split into four, as shown by the schematic diagram at the top. Spectrum (c) was obtained from a different electron spin, which is only coupled to a ^{14}N.

III. ELECTRON, ^{14}N AND ^{13}C

As one example of the conditional gate operation U_2, we use it for selective population transfer in a three-spin system consisting of the electron, the ^{14}N, and one ^{13}C nuclear spin: We swap the $m_S = 0$ and $m_S = -1$ states of the electron spin, conditional on the ^{14}N spin being in the $m_I = 0$ state, but independent of the ^{13}C spin. Figure 4(a) shows the spectrum of the electron spin, obtained from an FID experiment. The interaction with the ^{13}C nuclear spin splits each resonance line of the electron-^{14}N spin system into four lines. The splitting into four, rather than the usual $2I + 1 = 2$ lines results from the fact that the strength of the ^{13}C hyperfine interaction (≈150 kHz) is comparable to the nuclear Zeeman interaction (Larmor frequency $\nu_L = 165$ kHz) under our experimental conditions. The nuclear spin quantisation axis therefore points in different directions, depending on the state of the electron spin. As a result, the "usual" selection rule $\Delta m_S = \pm 1$, $\Delta m_I = 0$ for allowed ESR transitions cannot be applied and all possible transitions have a nonvanishing amplitude [26,27]. Details are given in the Appendix. Figure 4(b) shows the simulated spectrum, with the couplings shown in the panel at the top of the figure.

An effective population transfer requires that the ^{14}N nuclear spin controls the evolution of the electron spin, with little perturbation from the ^{13}C spin. In our experiment, the coupling from the passive spin is not negligible, in contrast to previous experiments, where there was no passive spin [28],
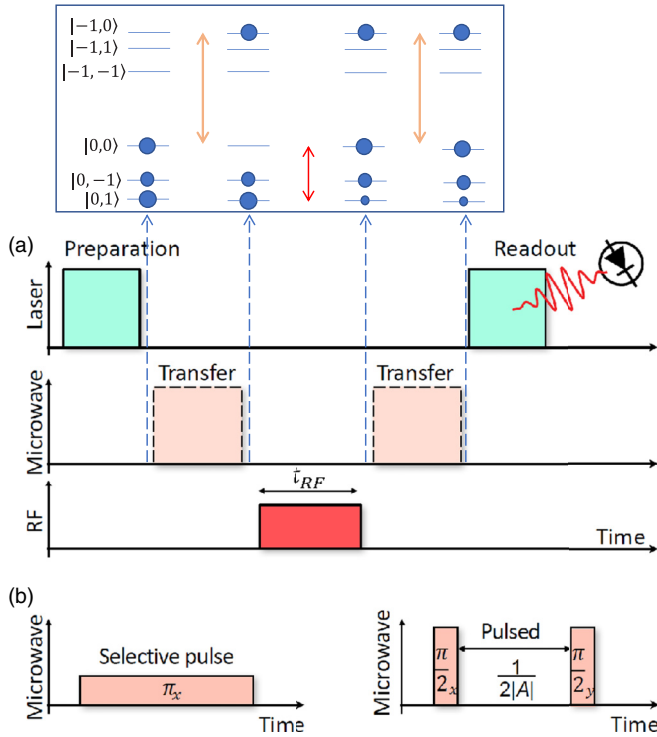
FIG. 5. (a) Pulse sequence for measuring the nuclear spin Rabi frequency. The carrier frequency of the RF pulse is resonant with the NMR transition $|0,0\rangle \leftrightarrow |0,1\rangle$, as indicated by the vertical short double arrow. The inset illustrates the state of the system during the experiment. The sizes of the filled circles are roughly proportional to the populations. The first transfer operation polarizes the nuclear spin, and the second acts as a readout to measure the remaining population after the RF pulse. (b) The MW pulses used for the population transfer between the two states marked by the long vertical arrows in the inset. The left-hand part shows the selective pulse used in previous works [6,28] and the right-hand part the pulse sequence used in the present work. In the selective pulse method, the Rabi frequency of the MW pulse is about 0.2 MHz, while the pulsed transfer uses hard pulses, with Rabi frequencies of about 10 MHz.

or the coupling from the passive spin was negligibly small compared to the active spin [6]. Compared to the conventional technique, the pulsed transfer reduces these perturbations.

As an application of the pulsed population transfer, we use it to polarize the ^{14}N nuclear spin, as shown in Fig. 5. After the transfer, we measure the Rabi frequency of the ^{14}N spin by applying a constant radio-frequency (RF) field of variable duration t_{RF}. After the RF pulse, we use another conditional gate operation for transferring the remaining nuclear spin polarization back to the electron spin for detection.

The experiments were implemented in a ^{12}C enriched (99.995%) diamond sample synthesized by chemical vapor deposition (CVD), where decoherence due to ^{13}C nuclear spins is small and the coherence time of the electron spin is $\approx 20 \, \mu s$ [29,30]. To evaluate the effect of the passive ^{13}C spin, we compare two centers, one with and one without the ^{13}C. The NV axes of the two centers point in the same direction, and the NMR transition frequencies in the concerned subspace $\{m_S = |0\rangle, |-1\rangle\}$ for these two centers were 4.981, 4.905, 2.822, and 7.075 MHz, for the transitions be-
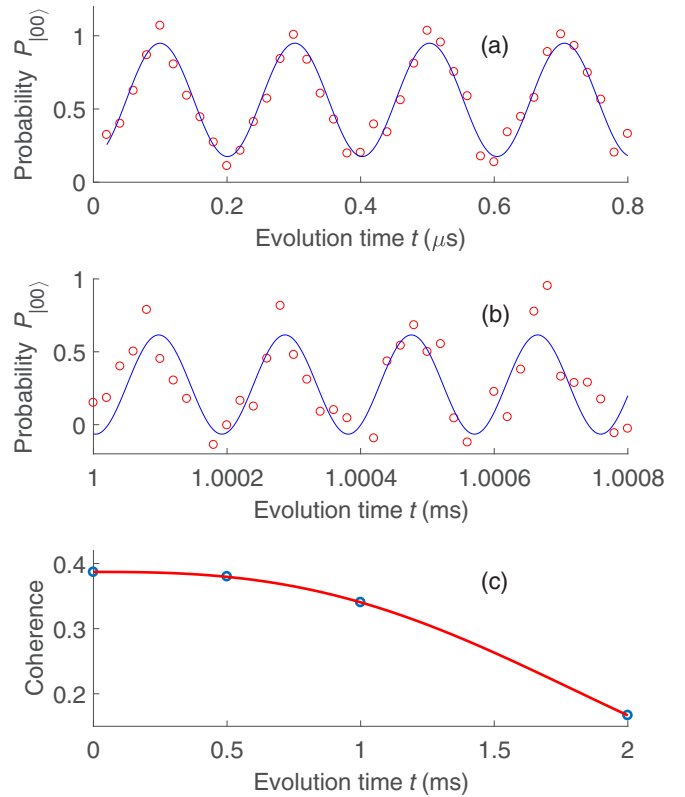

FIG. 6. Experimental results for the measurement of T_2^* for ^{14}N. (a-b) Population of the state $|0,0\rangle$ measured in the FID experiments for two different time periods. The measured data and fitting results are indicated by circles and solid curves. (c) Coherence amplitude extracted from the FID experiments versus time. Fitting the measured data to the function $A_0 e^{-(t/T_2^*)^k}$, we obtained $T_2^* = 2.1$ ms, $A_0 = 0.39$, and $k = 2.7$.

tween the states $|0,0\rangle \leftrightarrow |0,1\rangle$, $|0,0\rangle \leftrightarrow |0,-1\rangle$, $|-1,0\rangle \leftrightarrow |-1,1\rangle$ and $|-1,0\rangle \leftrightarrow |-1,-1\rangle$. Figure 4(c) shows the spectrum obtained from the electron spin without a coupled ^{13}C. For both centers, we performed measurements with the two different transfer techniques.

We measured the transverse relaxation time T_2^* for the ^{14}N nuclear spin via an FID experiment [6,28]. In the measurement, the MW and RF pulses were transition-selective, resonant with the transitions $|0,0\rangle \leftrightarrow |-1,0\rangle$ and $|0,0\rangle \leftrightarrow |0,1\rangle$, respectively. To measure the dephasing as the decay of the coherence, we performed partial FID measurements, for periods of $0.8 \, \mu s$ each, at different starting times. Figure 6 shows the experimental results. The two upper traces show partial FIDs, for different initial pulse separations, and the bottom trace plots the extracted amplitudes of the oscillation versus the initial evolution time for the four experiments. Fitting the coherence amplitudes to the function $A_0 e^{-(t/T_2^*)^k}$, we obtained $T_2^* = 2.1$ ms, $A_0 = 0.39$, and $k = 2.7$. The observed value of T_2^* is close to the longitudinal relaxation time $T_{1,e} \approx 3.5$ ms of the electron spin, which represents an upper limit for the measurement technique used here.

As a reference experiment, we first applied the pulse sequence used in earlier works to a center without coupled ^{13}C. The Rabi frequency of the MW pulses was 0.19 MHz, with the carrier frequency set to the transition between the $|0,0\rangle$ and
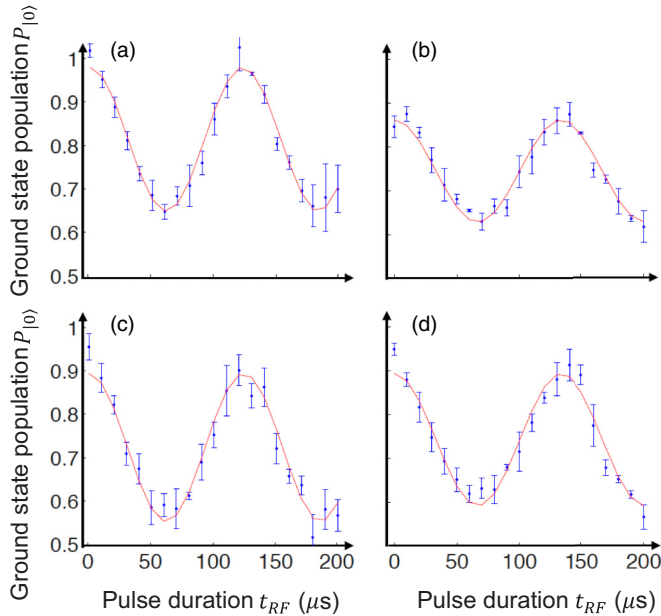
FIG. 7. Results of ^{14}N Rabi experiments in the NV centers without and with coupled ^{13}C, shown as left and right columns, from previous (top) and the new sequence introduced here (bottom).

$|-1, 0\rangle$ states. The frequency of the RF pulse was 4.981 MHz. The experimentally measured nuclear spin Rabi nutation is shown in Fig. 7(a), together with a fit to the function

$$P_{|0\rangle} = \alpha + \beta \cos(2\pi \nu_R t_{RF}), \qquad (8)$$

where ν_R denotes the Rabi frequency for ^{14}N, and α and β are constants. Table II shows the parameter values obtained by fitting the experimental data. Here we chose Fig. 7(a) as a reference for evaluating the following experiments.

Figure 7(b) shows the results obtained from the center with a coupled ^{13}C, from the previous pulse sequence in Fig. 5, where the Rabi frequency of the two MW pulses is 0.21 MHz. Comparison with Fig. 7(a) shows that the signal was degraded by the couplings from ^{13}C, resulting in a loss of signal by 12% and a decrease of the oscillation amplitude of 29%, since the Rabi frequency of the MW pulses is not large enough compared with the splitting caused by ^{13}C, which is about 0.15 MHz.

Figures 7(c)–7(d) show the results obtained from our modified sequence shown in Fig. 5, applied to the centers without and with the coupled ^{13}C. Table II shows the fitted parameters. Comparing the values for Figs. 7(b) and 7(d) shows a significant advantage for the new pulse sequence, which increases the oscillation amplitude of the signal by 21%. This

TABLE II. Fit results from the experimental data shown in Figs. 7(a)–7(d).

	α	β	ν_R (kHz)
Fig. 7(a)	0.816	0.164	8.2
Fig. 7(b)	0.743	0.117	7.5
Fig. 7(c)	0.723	0.168	8.1
Fig. 7(d)	0.742	0.151	7.5

advantage can be traced to the reduced effect of the coupling to ^{13}C due to the faster operations. The infidelity caused by the coupling from ^{13}C is reduced by $\sim A/\nu_{1,MW} > 10$, where $\nu_{1,MW} = 0.21$ MHz is the Rabi frequency of the transition selective MW π pulses in Fig. 5.

IV. CCNOT GATE

^{13}C nuclear spins close to NV centers are interesting candidates for qubits [31], provided effective gate operations can be implemented. If the hyperfine coupling is strong, two-qubit gates can be implemented by transition-selective pulses [6]. However, if multiple qubits are required, such as for the implementation of quantum error correction, it also becomes important to control more remote ^{13}C spins [5,32]. In these cases, selective pulses result in long gate times and as a result, the coherence time of the electron spin limits the fidelity of the overall gate operation. The pulsed scheme discussed above results in significantly shorter gate times and can thus alleviate this problem.

In this section, we still consider a system consisting of one electron, one ^{14}N, and one ^{13}C spin. We implement a CNOT in the electron-^{13}C system, with the additional constraint that the ^{14}N nuclear spin is in the state $m_I = 1$. In the three-spin system, this operation is a CCNOT gate or Toffoli gate [2], where ^{13}C and ^{14}N are the control spins, and the electron spin is the target. Since our scheme to implement the CNOT relies only on the secular component $A_{13C_{zz}}$ of the hyperfine interaction, we choose a center with $|A_{13C_{zx}}| \ll |A_{13C_{zz}}|$, for which the quantization axis is close to the NV axis [33]. In this case, the hyperfine coupling from the ^{13}C splits each peak of the electron-^{14}N system into two; details are given in the Appendix. With the field along the NV axis, we can approximate the relevant interaction Hamiltonian between the electron and ^{13}C as

$$\frac{1}{2\pi} \mathcal{H}_c = A_{13C_{zz}} S_z s_z, \qquad (9)$$

where s_z denotes the z component of the ^{13}C nuclear spin operator.

The experiments described here were done with the same ^{12}C enriched sample as those in Sec. III, but with a different NV center, with $T_2^* \approx 10 \,\mu$s. Figures 8(a) and 8(c) show the electron spin spectra obtained through FID measurements in the $m_S = 0$ and $m_S = \mp 1$ manifolds, respectively. The number of resonance lines indicates that in this center, the hyperfine tensor component $A_{13C_{zx}}$ is <50 kHz and thus sufficiently small to be neglected. The splitting of the peaks indicates that $A_{13C_{zz}} \approx 150$ kHz. In the following, we consider two subspaces of the full Hilbert space, both of which correspond to two-qubit systems with one electron-spin qubit and one ^{13}C nuclear spin qubit, while the ^{14}N nuclear spin is in the $m_N = 1$ state. The first subspace is spanned by the states $m_S = 0$ and $m_S = -1$ of the electron and the second by the states $m_S = 0$ and $m_S = 1$. In these two subspaces, we implement two slightly different CNOT gates, with the electron spin as a target and the nuclear spin as the control qubit. In the first subspace, we use the control condition that the ^{13}C spin is in the $\downarrow$ state, in the second subsystem that it is in the state $\uparrow$. Table III summarises these gates.
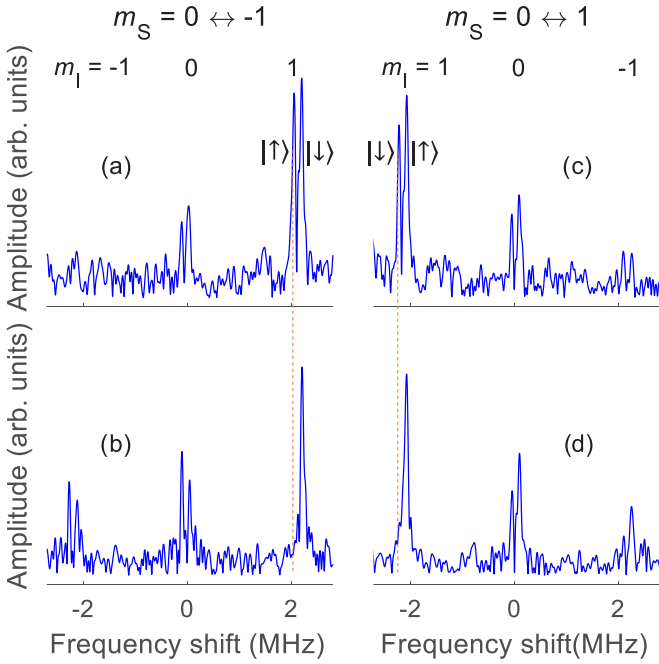
FIG. 8. Spectra of the electron spin coupled to one ^{14}N and one ^{13}C nucleus. The spectra in (a) and (c) are obtained from FIDs using MW pulses with the carrier frequencies set to the transition frequencies between states $m_S = 0$ and ∓ 1, and Rabi frequencies of 10 and 6 MHz, respectively. The spectra in (b) and (d) show the results obtained from the FID after the CNOT gates were implemented in the $m_S = 0$ and ± 1 manifolds with the ^{14}N in state $m_I = 1$, respectively. The states of the ^{13}C nuclear spin are indicated by $\uparrow$, $\downarrow$. The origin of the frequency axis in (a), (b) is the ESR transition frequency between the states $m_S = 0 \leftrightarrow -1$ ($D + \gamma_e B$), and in (c), (d) $m_S = 0 \leftrightarrow +1$ ($D - \gamma_e B$). The dashed vertical lines indicate the positions of the resonance lines where the nuclear spins are in the state that corresponds to the control condition: in this case, the gate operation flips the electron spin, which is verified by the fact that the corresponding peaks are absent in the spectra (b) and (d).

Figure 9 shows the pulse sequence used. The double arrows indicate the carrier frequencies of the MW pulses. The Rabi frequency of the pulses in the CNOT is 0.5 MHz. These two pulses are hard pulses for the electron and ^{13}C system, since the Rabi frequency is much larger than the coupling to ^{13}C, while they are selective with respect to the state of the ^{14}N. In order to observe the effects of the CNOT gate, we measured the FID signal. Figures 8(b) and 8(d) show the spectra of the

TABLE III. Output states of the electron (target) and ^{13}C (control) spins of the CNOT operations in the $m_S = 0$ and ∓ 1 manifolds, indicated as CNOT$_1$ and CNOT$_2$.

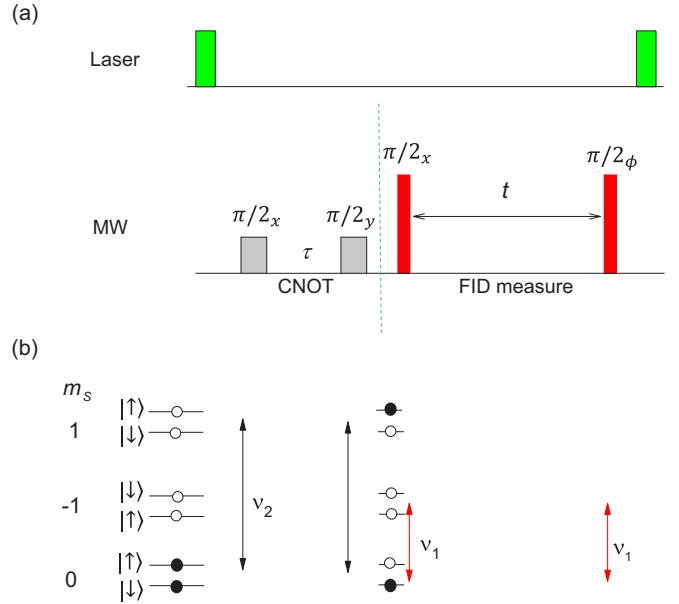| Input	Output of CNOT$_1$	Output of CNOT$_2$
1 $\uparrow$	1 $\uparrow$	0 $\uparrow$
1 $\downarrow$	1 $\downarrow$	1 $\downarrow$
0 $\uparrow$	0 $\uparrow$	1 $\uparrow$
0 $\downarrow$	-1 $\downarrow$	0 $\downarrow$
-1 $\uparrow$	-1 $\uparrow$	-1 $\uparrow$
-1 $\downarrow$	0 $\downarrow$	-1 $\downarrow$

FIG. 9. (a) Pulse sequence for demonstrating the CNOT gate implemented in the electron-^{13}C system. (b) Populations of the initial and final states when the CNOT gate is applied to subspace with $m_S = 0 \leftrightarrow -1$, $m_I = 1$. We therefore do not consider the ^{14}N spin here. The filled and empty circles denote population of 1/2 and 0, respectively. The states marked by $|\uparrow\rangle$ and $|\downarrow\rangle$ are the ^{13}C eigenstates. The carrier frequencies of the MW pulses are set to the transition frequencies between the $m_S = 0$ and 1 or -1, indicated as the lines with double arrows. ν_1 and ν_2 indicate the transition frequencies $D \pm \gamma_e B$, respectively. The Rabi frequencies of the MW pulses are 0.5 and 10 MHz in the CNOT gate and the FID measurement, respectively.

electron after the implementation of the CNOT gates in the $m_S = 0$ and $m_S = \pm 1$ manifolds, respectively. The single peak in the right or left transition of the ^{14}N multiplet verifies the operation of the CNOT gate, which transfers population from states $|0\uparrow\rangle$ to $|1\uparrow\rangle$, or $|0\downarrow\rangle$ to $|-1\downarrow\rangle$, respectively. We use the amplitude ratio between the single peak and the corresponding peak in the doublet to estimate the fidelity of the CNOT gate, and obtain values of 0.95 and 0.99 for Figs. 8(b) and 8(d), respectively.

If we use a transition-selective pulse to implement the CNOT gate, its Rabi frequency may not exceed 20 kHz if the theoretical fidelity should be at least 0.99 in the absence of dephasing effects. For such a low Rabi frequency, the duration of the π pulse becomes at least 25 μs, which is longer than the relaxation time $T_2^* \approx 10 \mu$s. Dephasing would thus reduce the fidelity of such a gate operation to ~ 0.6.

V. OFFSET DEPENDENCE

A. Narrow frequency range

The operations implemented by the $(\pi/2)_x - 1/2|A| - (\pi/2)_y$ pulse sequence depend strongly on the MW carrier frequency used to generate the pulses, as evidenced by the expression for U in Eq. (5). We therefore verified this dependence in the system consisting of the electron and ^{14}N nuclear spins by performing the gate operations as a function
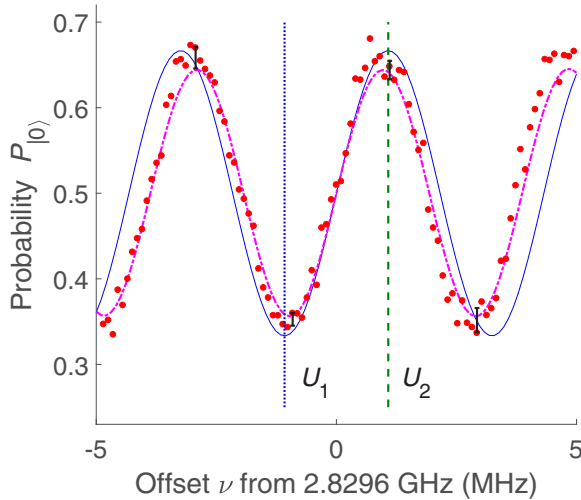
FIG. 10. Dependence of the operation U defined by Eq. (5) on the offset of the MW carrier frequency. The filled circles represent the experimental data, the full curve represents a simulation for ideal (δ-function) pulses, while the dash-dotted line was simulated with the pulse durations of $21.6\,\mu s$ used in the experiment. The blue dotted vertical line indicates the offset used for implementing U_1 and the dark green dashed line for U_2. The error bars represent the standard deviation of the measured data points.

of the carrier frequency and measuring the resulting ground state population. Applying the unitary of Eq. (5) to the initial state Eq. (7) yields ground state population

$$P_{|0\rangle} = \frac{1}{2} - \frac{1}{6}\sin\left(\frac{\pi\nu}{A}\right). \tag{10}$$

Figure 10 shows the results of this experiment performed in the sample with natural abundance. The vertical axis represents the population of the $m_S = 0$ state measured by the second laser pulse as a function of the offset of the MW carrier frequency, see Eq. (4). The dotted and dashed vertical lines indicate the offsets where the operation corresponds to U_1 and U_2, respectively. We compare the experimental results (filled circles) to a simulation of the experiment without dephasing effects, i.e., $T_2 \to \infty$, and using ideal pulses with infinite Rabi frequency of the MW pulses, shown as the full curve. The dash-dotted curve in the figure shows the result of a simulation for the actual Rabi frequency (11.6 MHz) used in the experiment, and $T_2 \to \infty$. It agrees well with the experimental data, indicating that T_2 effects are negligible in this experiment.

B. Wide frequency range

In addition to the data shown in Fig. 10, we also measured the offset dependence over the whole frequency range from 2.75 to 2.99 GHz to obtain the full offset dependence. Figure 11 shows the experimental results and compares them to a simulation that treats the nuclear and the electronic spins as spin-1 systems. Since the MW power at the sample varies as a function of frequency, we performed the experiment in two parts and set the duration of the $\pi/2$ pulses to $21.6\,\mu s$ in the low-frequency part and to $27.5\,\mu s$ in the high-frequency part. The two parts are separated by the dashed vertical line
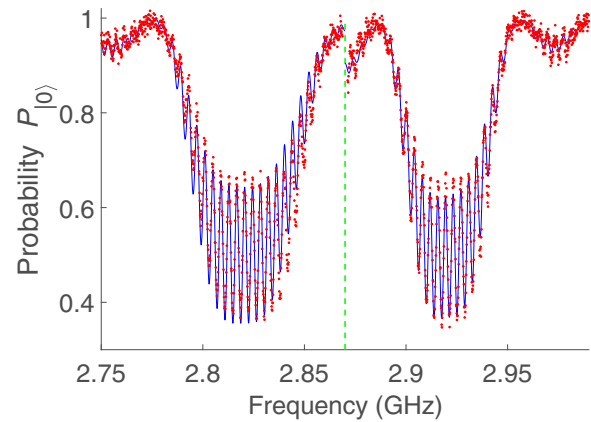

FIG. 11. Offset dependence of a CNOT gate with ^{14}N as control, comparing experimental results (dots) with a simulation (solid curve). The horizontal axis shows the carrier frequency of the MW. The scan consists of two segments, separated by the dashed line, where the pulse duration was changed.

in Fig. 11. The agreement between theory and experiment is best near 2.83 GHz and 2.93 GHz, where the calibration for the pulse duration was performed.

C. Transition-selective pulse

For comparison, we also implemented U_2 in the conventional way [7–10], using one low power pulse with a Rabi frequency of 0.23 MHz. Figure 12 shows the experimental and simulated results. The comparison between the experimental and simulated data shows that the T_2 effects cause $\sim 17\%$ loss of the fidelity of the gate, when it is implemented at offset 0.
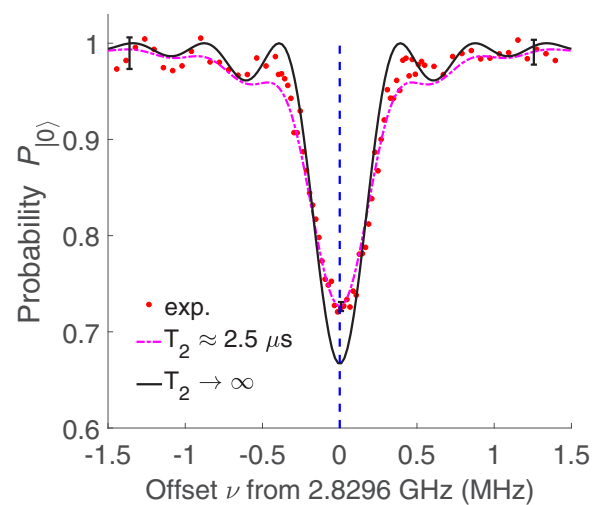

FIG. 12. Experimental results from a CNOT gate using a low-power pulse with a Rabi frequency of 0.23 MHz shown as circles. The dash-dotted and full curves show numerical simulations for the cases of $T_2 \approx 2.5\,\mu s$ and $T_2 \to \infty$. The dashed vertical line indicates the offset for implementing U_2.

VI. DISCUSSIONS AND CONCLUSIONS

The conventional method for implementing CNOT gates based on transition-selective pulses is an approximation [14], and the fidelity is limited by the spectral resolution of the system. Our results show that these limitations can be circumvented by using quantum gates based on hard pulses and free precession periods. The resulting gate duration is considerably shorter, which reduces the effects of relaxation. It allows us to implement a CNOT gate with an overall duration of < 300 ns in the electron and ^{14}N spin system, which is shorter than the pulse obtained by optimal control ($\sim$450 ns) [34], and much shorter than with a transition-selective pulse (1.8 μs) [8]. The gains are even bigger in the electron and ^{13}C spin system with the small coupling strength of $\approx$150 kHz, where the spectral resolution seriously limits the fidelity of gates based on transition-selective pulses.

In conclusion, our scheme for multiqubit operations provides significant improvements for quantum registers consisting of electronic and nuclear spins. The benefits include reducing the gate time and improving the control in the system with more couplings. The gates that we have chosen to implement here are important since they are members of the sets of gates required for universal quantum computing. Although we implemented the experiments in the NV center system at low magnetic fields, the method is completely general and can be applied to many other systems and higher magnetic fields.

APPENDIX

Here we consider a system Hamiltonian consisting of the electron and ^{13}C spins, by choosing the $m_I = 0$ subspace of the ^{14}N. The axis of the NV center and the position of the ^{13}C nucleus define a symmetry plane for the system [35] and we choose a symmetry-adapted coordinate system with the z axis along the NV axis, and the ^{13}C nucleus in the xz plane. The Hamiltonian can then be written as

$$\frac{1}{2\pi}\mathcal{H}_{E,C} = DS_z^2 - \nu_e S_z - \nu_L s_z + A_{13C_{zz}} S_z s_z + A_{13C_{zx}} S_z s_x.$$

(A1)

Here $s_{z/x}$ denote the z/x-components of the spin operator for ^{13}C, $\nu_e = \gamma_e B$, and $\nu_L = \gamma_C B$ with $\gamma_C = 10.7$ MHz/T.

We further restrict our system to the subspace spanned by the states $\{|0\rangle_e, |-1\rangle_e\} \otimes \{|\uparrow\rangle_C, |\downarrow\rangle_C\}$, where the Hamiltonian is

$$\frac{1}{2\pi}\mathcal{H}_{E,C}^{\text{sub}} = -\frac{1}{2}(D + \nu_e)\sigma_z - \left(\nu_L + \frac{1}{2}A_{13C_{zz}}\right)s_z$$
$$-\frac{1}{2}A_{13C_{zx}}s_x + \frac{1}{2}A_{13C_{zz}}\sigma_z s_z + \frac{1}{2}A_{13C_{zx}}\sigma_z s_x.$$

(A2)

Here, we have omitted the constant term $(D + \nu_e)E_4/2$, with E_4 denoting the identity in the four-dimensional space. σ_z denotes the z component of the Pauli matrices for the electron

spin. States $|\uparrow\rangle$ and $|\downarrow\rangle$ denote the eigenstates of s_z with eigenvalues $1/2$ and $-1/2$, respectively, and $|0\rangle_e$ and $|-1\rangle_e$ denote the eigenstates of σ_z with eigenvalues 1 and -1.

The Hamiltonian of Eq. (A2) can be diagonalized by the unitary transformation

$$U_T = |0\rangle\langle 0| \otimes E_2 + |-1\rangle\langle -1| \otimes R_y(\alpha),$$

(A3)

where E_2 denotes an identity operator for ^{13}C and

$$R_y(\alpha) = e^{-i\alpha s_y}$$

(A4)

with

$$\alpha = \arctan\left(\frac{A_{13C_{zx}}}{A_{13C_{zz}} + \nu_L}\right),$$

(A5)

indicating the orientation of the quantization axis of the ^{13}C spin in the subspace of $m_S = -1$. From the parameters $\nu_L = 165$, $A_{13C_{zz}} = -152$, and $A_{13C_{zx}} = 110$ kHz given in Fig. 4, we obtain $\alpha = 83°$.

From U_T, one obtains the eigenstates as $|0\uparrow\rangle$, $|0\downarrow\rangle$, $|-1\rangle[-|\uparrow\rangle\sin(\alpha/2) + |\downarrow\rangle\cos(\alpha/2)]$, and $|-1\rangle[|\uparrow\rangle\cos(\alpha/2) + |\downarrow\rangle\sin(\alpha/2)]$. The corresponding energies are

$$\frac{1}{2\pi}\mathcal{E}_1 = -\nu_L/2,$$

(A6)

$$\frac{1}{2\pi}\mathcal{E}_2 = \nu_L/2,$$

(A7)

$$\frac{1}{2\pi}\mathcal{E}_3 = \frac{1}{2}\nu_- + (D + \nu_e),$$

(A8)

$$\frac{1}{2\pi}\mathcal{E}_4 = -\frac{1}{2}\nu_- + (D + \nu_e),$$

(A9)

where

$$\nu_- = \sqrt{A_{13C_{zx}}^2 + (\nu_L + A_{13C_{zz}})^2}$$

(A10)

is the transition frequency of the ^{13}C spin in the subspace of $m_S = -1$.

The ESR transition frequencies between the levels $\mathcal{E}_k$ and $\mathcal{E}_l$, with $k = 3, 4$, and $l = 1, 2$, are

$$\nu_{3,1} = \frac{1}{2}(\nu_- + \nu_L) + (D + \nu_e),$$

(A11)

$$\nu_{4,1} = -\frac{1}{2}(\nu_- - \nu_L) + (D + \nu_e),$$

(A12)

$$\nu_{3,2} = \frac{1}{2}(\nu_- - \nu_L) + (D + \nu_e),$$

(A13)

$$\nu_{4,2} = -\frac{1}{2}(\nu_- + \nu_L) + (D + \nu_e),$$

(A14)

and the transition probabilities

$$\sin^2\left(\frac{\alpha}{2}\right), \quad \cos^2\left(\frac{\alpha}{2}\right), \quad \cos^2\left(\frac{\alpha}{2}\right), \quad \sin^2\left(\frac{\alpha}{2}\right), \quad (A15)$$

respectively.

[1] C. Brif, R. Chakrabarti, and H. Rabitz, New J. Phys. **12**, 075008 (2010).

[2] M. A. Nielsen and I. L. Chuang, *Quantum Computation and Quantum Information* (Cambridge University Press, Cambridge, 2000).

[3] J. Stolze and D. Suter, *Quantum Computing: A Short Course from Theory to Experiment*, 2nd ed. (Wiley-VCH, Berlin, 2008).

[4] D. Suter and F. Jelezko, Prog. Nucl. Magn. Reson. Spectrosc. **98-99**, 50 (2017).

[5] T. H. Taminiau, J. Cramer, T. van der Sar, V. V. Dobrovitski, and R. Hanson, Nat. Nanotech., **9**, 171 (2014).

[6] J. H. Shim, I. Niemeyer, J. Zhang, and D. Suter, Phys. Rev. A **87**, 012301 (2013).

[7] F. Jelezko, T. Gaebel, I. Popa, M. Domhan, A. Gruber, and J. Wrachtrup, Phys. Rev. Lett. **93**, 130501 (2004).

[8] J. Zhang and D. Suter, Phys. Rev. Lett. **115**, 110502 (2015).

[9] M. Hirose and P. Cappellaro, Nature **532**, 77 (2016).

[10] L. Robledo, L. Childress, H. Bernien, B. Hensen, P. F. A. Alkemade, and R. Hanson, Nature **477**, 574 (2011).

[11] L. M. K. Vandersypen and I. L. Chuang, Rev. Mod. Phys. **76**, 1037 (2004).

[12] R. Freeman, *Spin Choreography* (Oxford University Press, Oxford, 1998).

[13] R. R. Ernst, G. Bodenhausen, and A. Wokaun, *Principles of Nuclear Magnetic Resonance in One and Two Dimensions* (Oxford University Press, Oxford, 1990).

[14] T. F. Havel, S. S. Somaroo, W. Zhang, and D. G. Cory, Concepts in Magnetic Resonance Part A **23A**, 49 (2004).

[15] D. Suter and G. A. Alvarez, Rev. Mod. Phys. **88**, 041001 (2016).

[16] J. Zhang, A. M. Souza, F. D. Brandao, and D. Suter, Phys. Rev. Lett. **112**, 050502 (2014).

[17] C. S. Shin, M. C. Butler, H.-J. Wang, C. E. Avalos, S. J. Seltzer, R.-B. Liu, A. Pines, and V. S. Bajaj, Phys. Rev. B **89**, 205202 (2014).

[18] X.-F. He, N. B. Manson, and P. T. H. Fisk, Phys. Rev. B **47**, 8816 (1993).

[19] B. Yavkin, G. Mamin, and S. Orlinskii, J. Magn. Reson. **262**, 15 (2016).

[20] I. Chuang, N. Gershenfeld, M. Kubinec, and D. Leung, Proc. R. Soc. London A **454**, 447 (1998).

[21] F. Jelezko and J. Wrachtrup, Phys. Status Solidi A **203**, 3207 (2006).

[22] J. Meijer, B. Burchard, M. Domhan, C. Wittmann, T. Gaebel, I. Popa, F. Jelezko, and J. Wrachtrup, Appl. Phys. Lett. **87**, 261909 (2005).

[23] L. Childress, M. V. Gurudev Dutt, J. M. Taylor, A. S. Zibrov, F. Jelezko, J. Wrachtrup, P. R. Hemmer, and M. D. Lukin, Science **314**, 281 (2006).

[24] C. A. Ryan, J. S. Hodges, and D. G. Cory, Phys. Rev. Lett. **105**, 200402 (2010).

[25] P. Neumann, I. Jakobi, F. Dolde, C. Burk, R. Reuter, G. Waldherr, J. Honert, T. Wolf, A. Brunner, J. H. Shim, D. Suter, H. Sumiya, J. Isoya, and J. Wrachtrup, Nano Lett. **13**, 2738 (2013).

[26] N. Khaneja, Phys. Rev. A **76**, 032326 (2007).

[27] J. S. Hodges, J. C. Yang, C. Ramanathan, and D. G. Cory, Phys. Rev. A **78**, 010303 (2008).

[28] T. van der Sar, Z. H. Wang, M. S. Blok, H. Bernien, T. H. Taminiau, D. M. Toyli, D. A. Lidar, D. D. Awschalom, R. Hanson, and V. V. Dobrovitski, Nature **484**, 82 (2012).

[29] T. Teraji, T. Taniguchi, S. Koizumi, Y. Koide, and J. Isoya, Appl. Phys. Exp. **6**, 055601 (2013).

[30] J. Zhang, J. H. Shim, I. Niemeyer, T. Taniguchi, T. Teraji, H. Abe, S. Onoda, T. Yamamoto, T. Ohshima, J. Isoya, and Dieter Suter, Phys. Rev. Lett. **110**, 240501 (2013).

[31] J. Wrachtrup, S. Y. Kilin, and A. P. Nizovtsev, Opt. Spectrosc. **91**, 429 (2001).

[32] G. Waldherr, Y. Wang, S. Zaiser, M. Jamali, T. Schulte-Herbrueggen, H. Abe, T. Ohshima, J. Isoya, J. F. Du, P. Neumann *et al.*, Nature **506**, 204 (2014).

[33] A. Dreau, P. Spinicelli, J. R. Maze, J.-F. Roch, and V. Jacques, Phys. Rev. Lett. **110**, 060502 (2013).

[34] J. Geng, Y. Wu, X. Wang, K. Xu, F. Shi, Y. Xie, X. Rong, and J. Du, Phys. Rev. Lett. **117**, 170501 (2016).

[35] K. R. K. Rao and D. Suter, Phys. Rev. B **94**, 060101 (2016).